Haze Particle Nucleation Simulations in Cirrus Clouds, and Applications for Numerical and Lidar Studies

KENNETH SASSEN AND GREGORY C. DODD

Department of Meteorology, University of Utah, Salt Lake City, Utah

(Manuscript received 31 October 1988, in final form 26 April 1989)

ABSTRACT

A one-dimensional cloud microphysical model is applied to exploring the basic conditions under which ice crystal nucleation, from the homogeneous freezing of ammonium sulfate haze particles, can occur in cirrus clouds at temperatures $\leq -35°C$. Cirrus generating regions maintained by uniform updrafts of 0.1–0.25 m s^{-1}, and an idealized ice crystal precipitation mechanism dependent on vertical wind shear are treated in the model. The findings indicate that ice crystals are generated in a pulse-like fashion as a result of water vapor competition effects from ice crystals nucleated within an updraft, followed by precipitation. Water saturation is not required for ice crystal nucleation at $\leq -35°C$, and the relative humidities required at decreasing temperatures gradually decrease. The temperature dependency of the relative humidities associated with ice production does not depend significantly on model inputs, suggesting that cirrus cloud processes follow an adjusted pseudoadiabat, which produces ice mass contents that become increasingly smaller than those possible from a pseudoadiabatic process involving nucleation at water saturation. Finally, to determine whether polarization lidar observations can identify haze particles in cirrus generating regions, as has been suggested by recent studies, Mie scattering simulations were performed for the properties of the model-generated haze particles.

1. Introduction

In a previous study (Sassen and Dodd 1988), a mixed-phase hydrometeor growth model was applied to explaining the glaciation of a highly supercooled liquid layer observed jointly by ground-based polarization lidar and aircraft probes at the base of an orographic cirrus cloud. At temperatures between about $-35°C$ and $-37°C$, it was shown that the experimental findings could be reconciled with model simulations when ice crystals were nucleated through the homogeneous drop freezing mode. Cloud droplet solution effects on drop freezing and growth were treated using droplet populations formed from ammonium sulfate cloud condensation nuclei (CCN). At these cold temperatures, cloud glaciation occurred quite rapidly, and thus it was sufficient to employ a 200 m height domain in the time-dependent, one-dimensional model. In terms of the homogeneous nucleation rate J_{ls}^*, predicted by classical theory, a rate of $(1.5 \times 10^6) J_{ls}^*$ cm^{-3} s^{-1} was found to maximize the agreement between theory and measurement.

In the current work, we are concerned with the factors controlling cirrus cloud development above the previously limited model height domain and at still colder temperatures. On the basis of lidar studies (Platt and Dilley 1981), it is clear that the majority of cirrus cloud tops extend above the approximate $-40°C$ temperature level that marks the onset of rapid drop freezing through the homogeneous mode. In particular, we shall examine the behavior of haze particles within cirrus to define, to a first-order approximation, their role in ice particle nucleation. Our previous simulations have illustrated that haze particle populations can be created from cloud droplets that evaporate due to vapor competition effects from the initial ice crystals nucleated near the cloud base. The presence of this residual solution droplet component after cloud glaciation was indicated by a slight decrease in the lidar linear depolarization ratio δ below that expected for the pure ice phase cloud, and recent lidar cirrus measurements have suggested that embedded convective regions display low δ values (relative to the surrounding cloud) as a result of the scattering contributions from rapidly growing haze particles, the precursors of new ice crystals (Sassen et al. 1989).

To investigate the fundamental cloud microphysical processes within the homogeneous drop freezing temperature regime, our mixed-phase cirrus growth model has been modified to account for ice particle ventilation and fallout effects. Although still retaining the framework of a one-dimensional model, the effects of vertical wind shear are parameterized in such a way as to approximate the loss of ice mass due to sedimentation from a rising column. Our intention has not been to numerically reproduce a specific set of cirrus cloud ob-

Corresponding author address: Dr. Kenneth Sassen, Dept. of Meteorology, University of Utah, 819 Wm. C. Browning Bldg., Salt Lake City, Utah 84112.

servations as in Sassen and Dodd (1988), but rather to examine the general conditions under which new ice particle generation is possible within cirrus clouds. Our findings will then be applied to evaluating the inferences drawn from lidar depolarization observations, and are also directed toward the development of a parametric treatment of realistic ice particle generation for incorporation in large-scale cirrus cloud growth models as in, e.g., Starr and Cox (1985), in which microphysical, dynamical, thermodynamical, and radiative processes are allowed to fully interact.

2. The cloud model

The cloud microphysical model employed in this study is a modification of the one-dimensional model used in Sassen and Dodd (1988). As in the previous study, the model treats mixed-phase microphysics, with ice nucleation occurring solely through the homogeneous freezing mode, and includes thermodynamic equations. An important aspect of this model is the inclusion of solution effects in the computation of an effective temperature for the calculation of the probability of drop freezing. The growth of each ice crystal nucleated is treated individually such that a size distribution of particles is generated. Ventilation effects are now included in the formulation for ice crystal growth, as in Hall and Pruppacher (1976). The mass growth equation uses an ice density of 0.9 g cm^{-3} to simulate a hollow-ended column crystal, which is modeled as a prolate spheroid with a 2 to 1 axis ratio. The particle terminal velocity U_∞ is computed as in Davis (1974, Table 3.11) from $U_\infty = (7.31 \times 10^{-3})L^{1.415}$, where L is the length of the major axis. Additionally, as described below, a highly parameterized precipitation mechanism has been incorporated into the model framework.

Since cirrus clouds develop within regions of the upper troposphere that chracteristically display vertical shear in the horizontal winds, which evidence suggests can significantly affect cirrus cloud formation (Heymsfield 1977; Sassen et al. 1989), it is important to numerically treat the effects of wind shear on the development of deep cirrus clouds. Our approach to modeling cirrus generating regions is illustrated schematically in Fig. 1, which portrays the structure of an idealized cloud impulse of constant vertical velocity W in an environment with vertical wind shear. The environment is assumed to be a diffuse cirrostratus cloud containing ice crystal concentrations that are relatively insignificant in relation to those generated within the updraft. (For the initial set of simulations designed to assess the impact of basic nucleation processes on cirrus, no ice particle entrainment into the rising column is permitted.) The boundaries of the hypothetical impulse are determined by two offset parabolas with x_0 representing the radius of the disturbance. In the present formulation of the one-dimensional

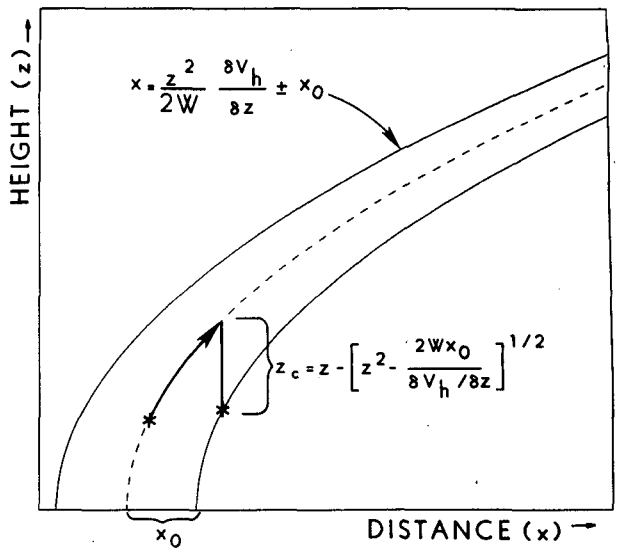

FIG. 1. Schematic portrayal of an idealized cirrus cloud impulse of vertical velocity W and radius x_0 subject to a vertical wind shear rate of $\partial V_h/\partial z$. The impulse is defined by two offset parabolas (top equation), and z_c represents the critical distance that an ice crystal must fall to sediment out of the impulse.

model, ice crystals are considered to remain within the forecast cloud volume until the particles sediment entirely out of the impluse. The net loss of ice crystals from the impulse at each forecast height is assumed to be zero unless the total distance z_c fallen by an ice crystal i) exceeds the vertical distance between the center line and the lower boundary of the impulse, as schematically shown in Fig. 1, or ii) exceeds the distance to the base of the cloud. That is, when the condition

$$\int_t U_\infty(t')dt' > z_c$$

is fulfilled, the ice crystal has precipitated. In Fig. 2, the critical fall distance z_c is shown as a function of height above cloud base z' for three vertical wind shear rates. The linear increase found in the lower cloud regions reflects a loss of ice crystals through the base of the cloud.

The model utilizes a time step of 0.01 s to ensure numerical stability under the unusual microphysical conditions encountered in the simulations. In all cases, the initial conditions simulated at cloud base were a temperature of −40°C, a pressure of 350 mb, and a relative humidity of 96.5%. Constant vertical velocities between 0.1 to 0.25 m s^{-1} were chosen to represent average ascent rates associated with generating cells embedded within cirrostratus, similar to those reported by Heymsfield (1977) for cirrus uncinus. Vertical wind shears of from 1.0 to 10 m s^{-1} km^{-1} were employed, encompassing the range of $\partial V_h/\partial z$ recently reported for three cirrus cloud case studies by Sassen et al.

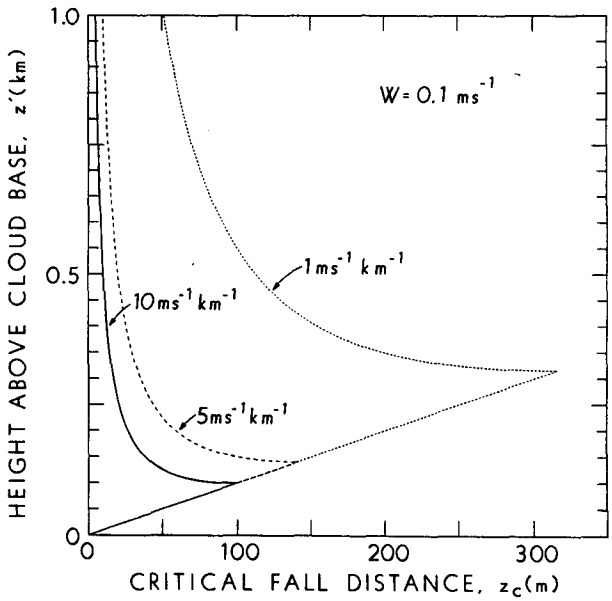

FIG. 2. The dependence of the critical fall distance z_c on height above cloud base z' for three wind shear rates, a constant vertical velocity of 0.1 m s^{-1}, and an impulse radius of 0.5 km.

(1989). The diameter of the impulse, $2x_0$, is 1.0 km, based on the observations of single cirrus generating cells by Heymsfield (1977), and the observations of Sassen et al. (1989). Since there is little knowledge of the size distributions of CCN in the upper troposphere, rather than attempt to specify a CCN distribution, we have adopted the approach of treating a wide range of CCN masses composed of ammonium sulfate. Five distinct classes of CCN with masses ranging from 10^{-12} to 10^{-16} g in decade steps are considered, where the radii of the dry particles range from 0.51 to 0.024 μm, respectively. The total CCN concentration treated in the model is arbitrarily specified at 100 cm^{-3}, with equal numbers of CCN from each of the classes used in a simulation. Although the model imposes minimum haze particle sizes consistent with those of droplets with molalities approaching the saturation level, ice nucleation occurs only for those drops whose molality is significantly less than saturated.

3. Haze particle nucleation and vertical cloud development

Initial model simulations were designed to evaluate the effects of varying the vertical wind shear on the formation of cirrus particles within a rising column, and neglected any effects from a background concentration of ice crystals. A constant updraft velocity of $W = 0.1$ m s^{-1} was specified, and the model was run for wind shear rates $\partial V_h/\partial z$ of 1, 5, and 10 m s^{-1} km^{-1} through a cloud depth of 1.0 km using all five CCN mass classes. The results are given in Figs. 3 and 4 for properties found within the impulse, and in Fig. 5 for the accumulated precipitation produced by this process. Note that the predictions in Fig. 5 are shown at the height above cloud base that the sedimenting particles emerge from the lower boundary of the impulse or precipitate out through the cloud base at $z' = 0$, and that the data values for precipitation are normalized to the specific volume determined by the cloud base air density. The temperature scale provided for reference in Fig. 5 illustrates that the average model generated lapse rate is 9.34°C km^{-1} within our simulated cirrus clouds.

The chief finding from Fig. 3 is that ice crystals are generated in a pulse-like fashion within a uniform updraft, with the relative frequency of generation events above the cloud base region increasing as the amount

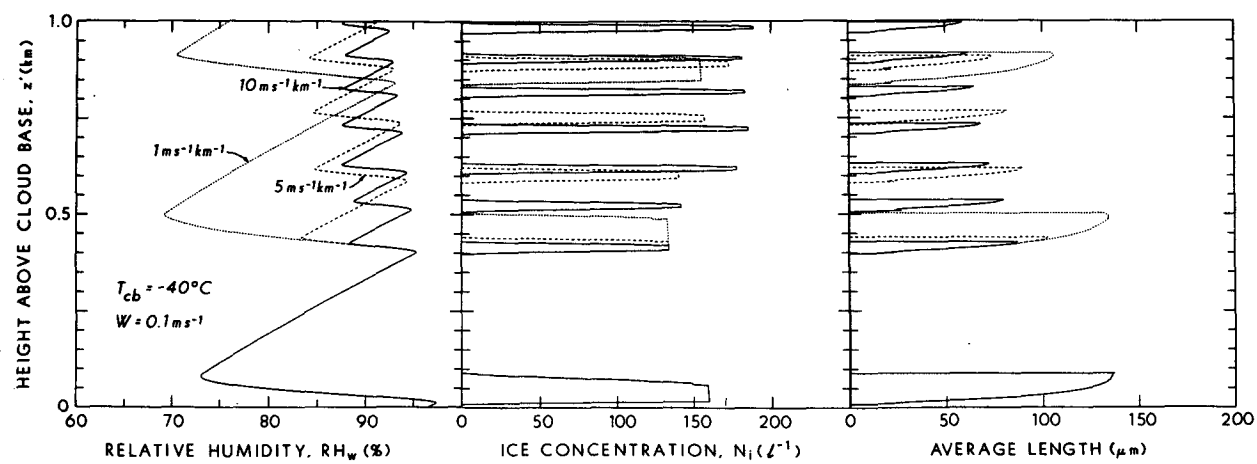

FIG. 3. Model results over a 1-km cloud depth for a 0.1 m s^{-1} updraft and the three indicated wind shear rates, in terms of (a) relative humidity with respect to water RH_w, (b) ice crystal concentrations N_i, and (c) average column crystal length. Maximum CCN masses of 10^{-12} g were used, and no ice crystal entrainment into the impulse was permitted. The cloud base temperature T_{cb} of −40°C is used in all simulations.

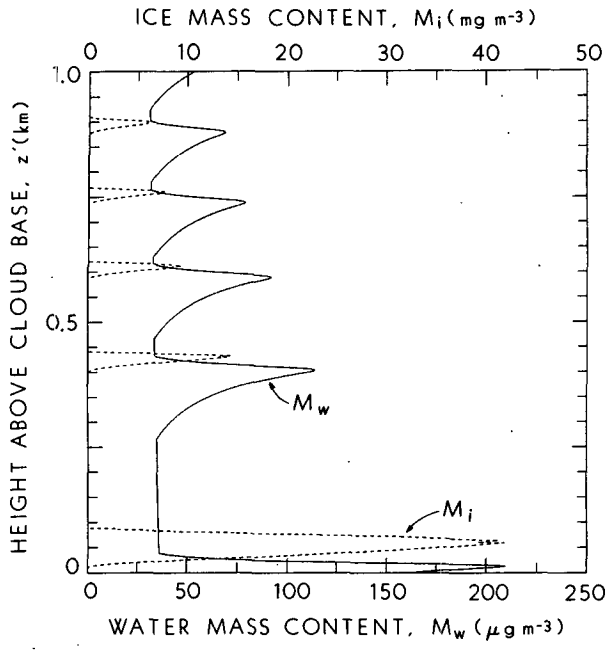

FIG. 4. Vertical distribution of ice M_i and water M_w mass contents corresponding to the 5 m s^{-1} km^{-1} shear rate data of Fig. 3 showing the effects of ice crystal vapor competition effects on haze particle growth. The flat troughs in the M_w curve reflect the use of minimum haze particle sizes consistent with the approach of solute saturation levels.

of vertical wind shear increases. This behavior results from the fact, as shown in Fig. 4, that the gradual growth of haze particles within the updraft following the fallout of ice crystals is abruptly reversed by the vapor competition effects produced by the growth of new ice crystals nucleated homogeneously. The generation of a sufficient number of ice crystals to cause a slight reduction in relative humidity effectively terminates the nucleation process, until crystal fallout again occurs and the sequence is repeated. The vertical distance over which ice nucleation is completed in these simulations is ~9 m (90 s at the 0.1 m s^{-1} updraft) for each generating pulse, with the peak relative humidity occurring at about the time that one half of the crystals have nucleated. Examination of the individual nucleation events reveals that it is predominantly the haze particles derived from the largest CCN mass that consistently freeze in the pulses, with, e.g., ~98% of the ice crystals in Fig. 5a derived from the 10^{-12} g CCN class. Although ice mass contents M_i and average crystal lengths L tend to decline with increasing height, the ice crystal concentrations N_i tend to increase within successive pulses. As shown in Fig. 5b, the accumulated precipitation mass tends to be conserved at each wind shear rate despite the considerable differences in the ice generating properties of the pulses, as required by thermodynamic considerations. Note that, at this updraft velocity, the initial precipitation from the first generation pulse occurs through cloud base.

It is apparent from Fig. 3a that the peak saturations found in each ice crystal generating pulse gradually decrease with decreasing temperature, and are quite similar regardless of the wind shear rate. This suggests that ice crystal generation within the homogeneous nucleation regime may be accomplished under prescribed environmental conditions, although the effects produced by varying the updraft velocity and the CCN mass distribution must also be evaluated. Hence, shown in Figs. 6 and 7 are simulations performed at a

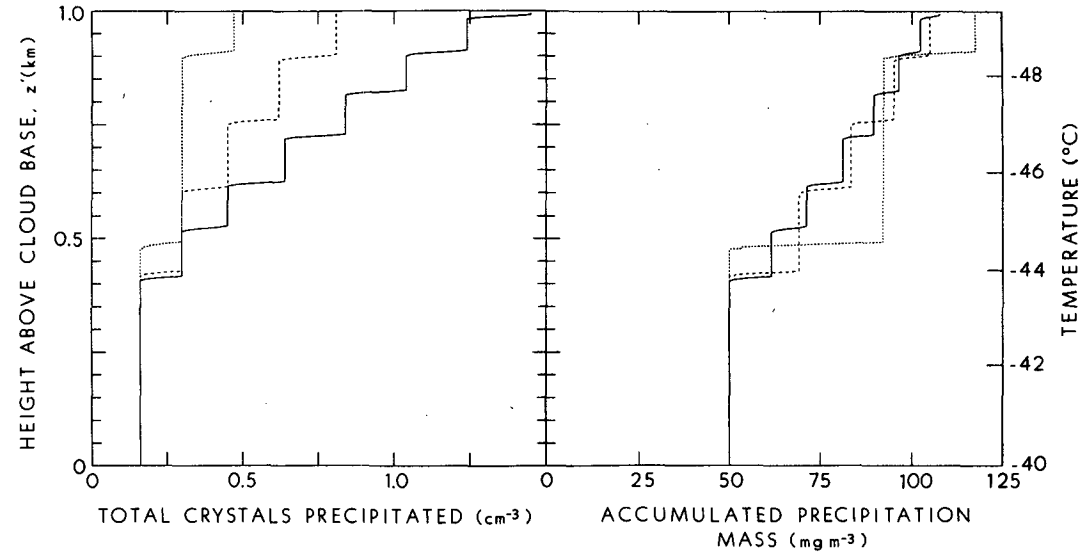

FIG. 5. Model results for the accumulations with height of the (a) concentrations, and (b) mass contents of ice crystal precipitation from the impulses corresponding to the three sets of curves in Fig. 3. The model-generated temperature gradient is shown at right.

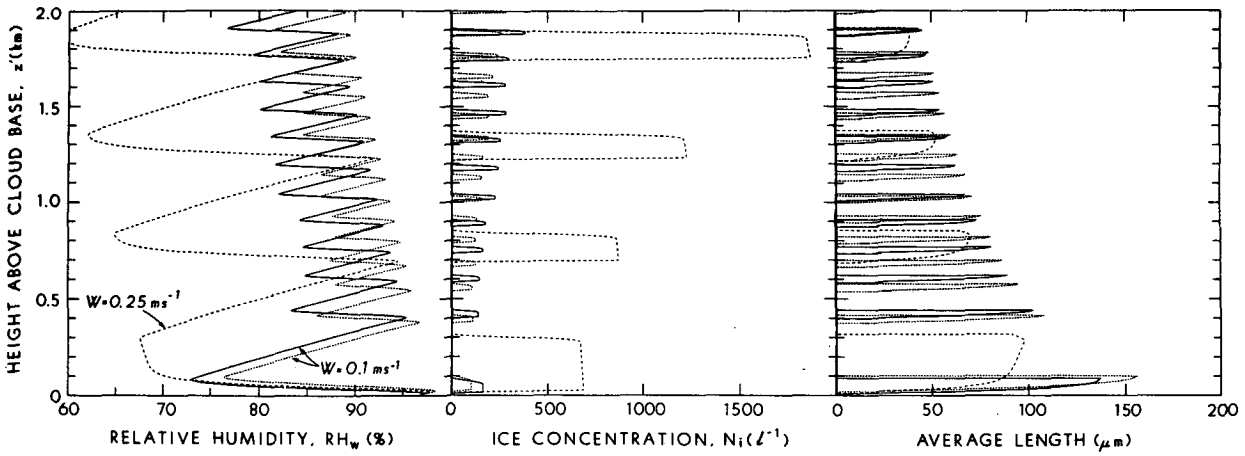

FIG. 6. Model results obtained over a 2-km cloud depth for the same quantities as in Figs. 3a–c, but using 0.1 and 0.25 m s^{-1} updraft velocities and maximum CCN masses of 10^{-12} g (solid and dashed curves) and 10^{-14} g (short-dashed curves). All curves are for a 5 m s^{-1} km^{-1} wind shear rate and allow for no ice particle entrainment.

5 m s^{-1}/km wind shear rate over a 2.0 km cloud depth, where predictions at W = 0.1 m s^{-1} for maximum CCN masses of 10^{-12} g (solid curves) and 10^{-14} g are compared with those obtained using the full 10^{-12} to 10^{-16} g CCN spectra at W = 0.25 m s^{-1}, which likely represents a comparatively strong average updraft associated with deep cirrus generating regions. Significantly, although there are fewer ice generating pulses and much higher crystal concentrations produced by the 0.25 m s^{-1} updraft, the vertical distributions of peak relative humidities and the accumulated precipitation masses are rather similar for all three cases. The higher updraft velocity also prevents the initial precipitation from leaving the impulse through cloud base. As explored in section 4, the behaviors of the relative humidity and accumulated precipitation mass profiles revealed by these simulations provide significant insights into the fundamental processes controlling cirrus cloud formation.

In order to approximate the conditions in which the impulse is embedded in cirrostratus, simulations were performed after inserting at each time step a constant background concentration of 100 μm-long column crystals to mimic the entrainment of cirrus particles into the updraft. Model predictions in terms of relative humidity and the concentrations of nucleated crystals are given in Fig. 8 for background crystal concentrations of 1 and 5 L^{-1}. These values were selected on the basis of averaged aircraft data in cirrostratus at the appropriate temperatures (Sassen et al. 1989), and the

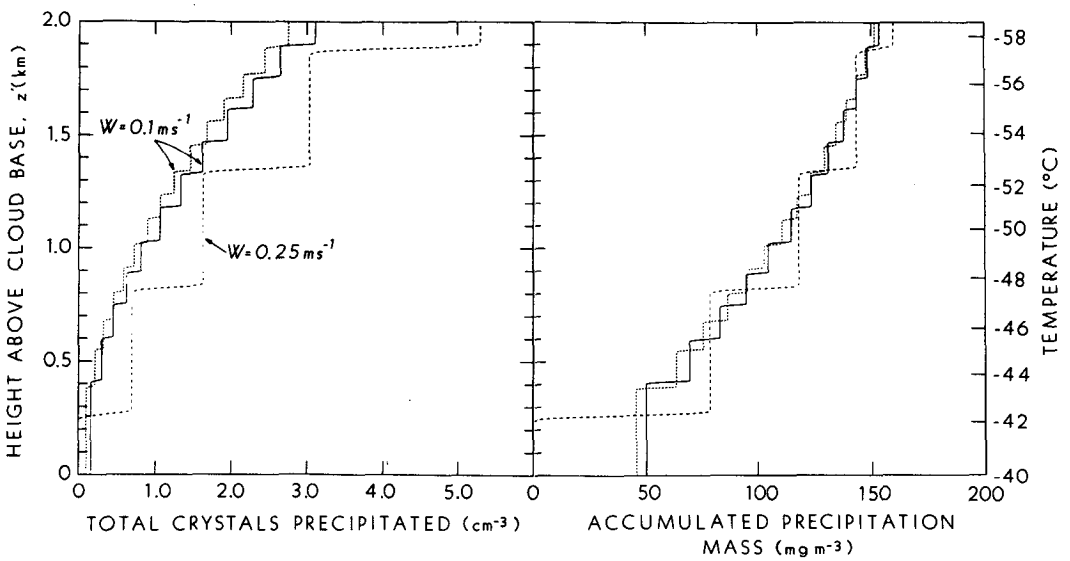

FIG. 7. Properties of the precipitated ice crystals, as in Fig. 5, corresponding to the three curves in Fig. 6.

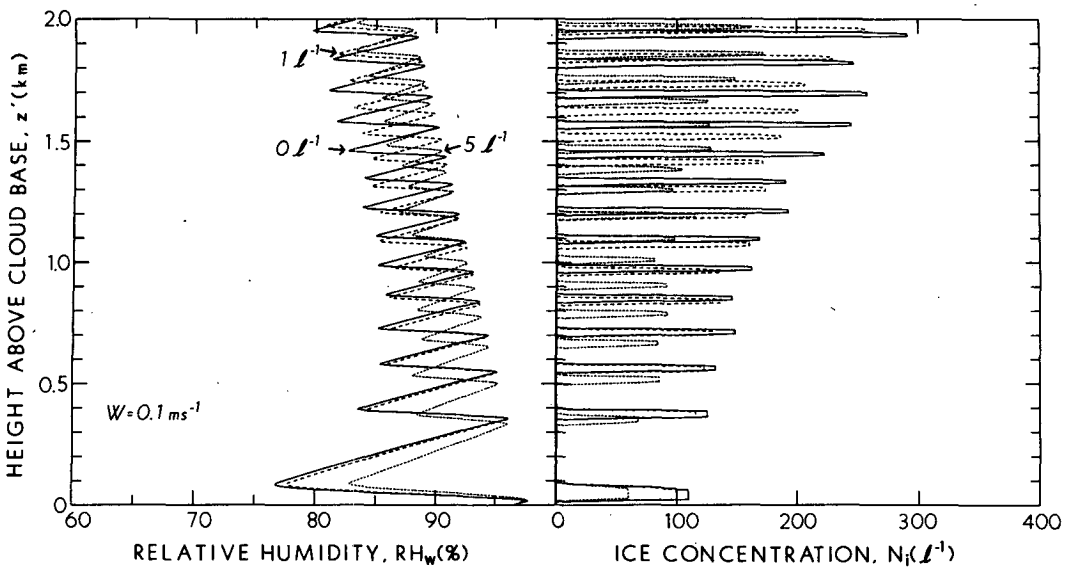

FIG. 8. Effects on the relative humidity and nucleated ice crystal concentrations produced by introducing a constant background of 100 μm-long crystals at concentrations of 0, 1, and 5 L^{-1}, mimicking the entrainment of crystals in cirrostratus into the impulse. A 5 m s^{-1}/km wind shear and maximum CCN mass of 10^{-13} g were used in these simulations.

case for no background crystals is given for comparison. Increases in the background crystal concentrations over this range cause the relative frequency of the ice generating pulses to increase. Since the background crystals act as an additional water vapor sink, stronger vapor competition effects occur during the start of the nucleation sequence, thereby reducing the total number of crystals formed in each pulse (Fig. 8b). The net result is similar to that of decreasing the vertical velocity. Nonetheless, the pulse-like generation of ice crystals in a uniform updraft remains an obvious feature of the simulated cirrus even under the typical background ice crystal conditions measured in cirrostratus.

4. Fundamental considerations and model applications

On the basis of these idealized model findings, some important generalizations regarding cirrus cloud generation, and their implications for numerical modeling efforts, can be inferred. In particular, the behavior of the relative humidity profiles in Figs. 3a, 6a, and 8 reveals a fundamental characteristic of ice crystal formation within cirrus clouds. As a result of the modulation of the homogeneous drop freezing rate by haze particle solution effects and the great importance of the vapor competition effects resulting from nucleation events, it is evident that the production of new ice particles through primary processes can occur only within a rather narrow domain in the temperature and humidity fields, i.e., under reasonably predictable ambient conditions. To illustrate the consequences of the temperature dependency noted in the relative humidity peaks generated by the cloud model, Fig. 9 is presented.

The domain contained within Fig. 9 is representative of the temperature-humidity field of importance to the generation of cirrus particles within the homogeneous nucleation regime. The solid curves crossing this do-

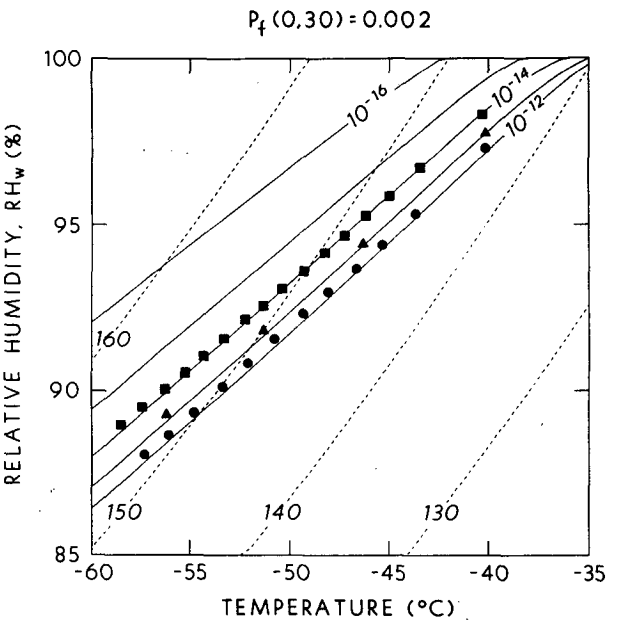

FIG. 9. The temperature and humidity dependence of ice crystal nucleation resulting from the homogeneous freezing of haze particles (solid lines) of the indicated CCN masses of ammonium sulfate, based on the probability of drop freezing P_f given at top. Data points are derived from the peak relative humidities produced within ice generating pulses under various model conditions (see text). Dashed lines refer to supersaturations (in percent) relative to ice.

main represent the environmental conditions under which equilibrium haze particles of the five ammonium sulfate CCN classes display a probability of freezing within a 30 s time interval of $P_f(0, 30) = 0.002$. A 30 s period was chosen to correspond to the approximate time involved in obtaining the peak relative humidity value following the initiation of ice crystal nucleation within each pulse, as well as being appropriate for a large-scale cirrus model time step. The low freezing probability reflects the dominance of ice crystal vapor competition effects, which greatly restricts the number of nucleations that can occur from an essentially unlimited haze particle population, with the 0.002 value based on the approximate number of crystals generated within each pulse in Fig. 6b (solid line) for $W = 0.1$ m s^{-1}. Hence, it should not be surprising that the relative humidity peaks derived from this model run (the solid circles in Fig. 9) should approximate the curve corresponding to the freezing behavior of the equilibrium haze particles derived from the 10^{-12} g CCN, the dominant class of nuclei involved in ice generation in this case. Similarly, the solid squares refer to the behavior of the RH_w curve in Fig. 6a for much smaller CCN (10^{-14} g maximum), which again show good agreement with the corresponding equilibrium haze particle curve. The remaining solid triangles, from the $W = 0.25$ m s^{-1} case in Fig. 6a, do not fit as closely with the appropriate 10^{-12} g curve because of the increased numbers of ice crystals nucleated at this vertical velocity, but still the differences are not very significant.

Although it is generally accepted that a water saturated environment is needed to nucleate ice particles in the troposphere (i.e., supercooled droplets are required due to a scarcity of sublimation ice nuclei), it is clear from Fig. 9 that the RH_w barrier that must be overcome to nucleate cirrus particles for temperatures colder than about −35°C is a function of temperature. Water saturation is no longer required, and cirrus clouds in essence become easier to produce with decreasing temperature insofar as reduced relative humidities are required to nucleate ice crystals. Furthermore, assuming that ample concentrations of CCN are available, i.e., in the 10^{-12} to 10^{-14} g categories, there is only a rather narrow domain in the temperature/humidity field within which new ice crystals can be generated. Consequently, the area beneath the applicable freezing probability curves represents a reservoir of stable haze particles or unactivated CCN; each curve is both a sink for haze particles and a source of ice crystals; and the area above the curves becomes, in effect, a forbidden domain analogous to that defined by the 100% relative humidity barrier for temperatures ≥ -35°C, which is rarely exceeded by more than a few percent in the atmosphere.

As a result of this finding, the production of precipitation in cirrus follows an adjusted pseudoadiabatic process characterized by a temperature lapse rate that lies between those of a water and ice saturated process.

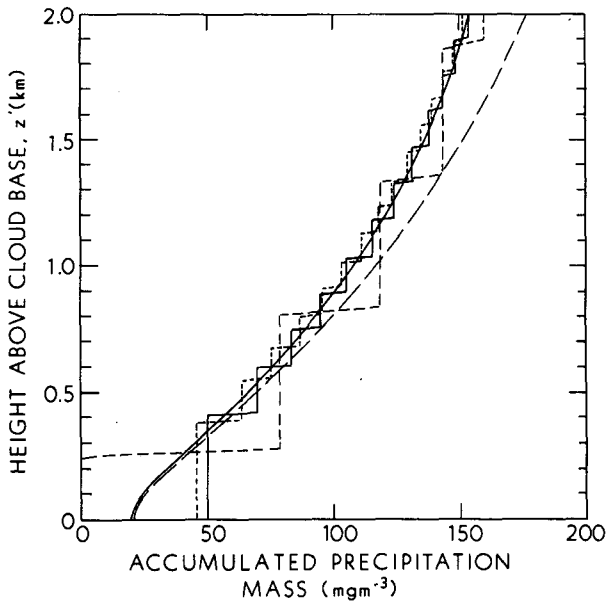

FIG. 10. Comparison of accumulated precipitation mass from the model simulations in Fig. 7b with those based on an adjusted pseudoadiabatic analysis (solid curve), which results from the effects of the boundary in the temperature/humidity domain for ice nucleation shown in Fig. 9, and on a more conventional pseudoadiabatic analysis (dashed curve).

Since water saturation at these temperatures cannot be attained, the decline in cirrus ice mass contents experienced with decreasing temperature is more rapid than that corresponding to the pseudoadiabatic rate involving nucleation at water saturation. As shown in Fig. 10, the rate at which precipitation ice mass accumulates can be predicted with regard to the curves in Fig. 9. For example, a linear fit to the solid circles in Fig. 9 provides a simple relation between cloud temperature and the maximum RH_w values produced under a given set of conditions. Employing the model-generated average temperature lapse rate of 9.34°C km^{-1}, the loss of water vapor content following a path along this curve when converted to ice mass (i.e., the solid line in Fig. 10) corresponds to the averaged accumulated precipitation mass for the three distinct model simulations. For comparison, the dashed curve in Fig. 10 represents the product of a pseudoadiabatic process appropriate for cirrus cloud growth in our model domain under water saturated conditions. Clearly, the differences become increasingly significant with decreasing temperature as the available water vapor reservoir associated with clouds attaining water saturation becomes increasingly under-utilized. The adjusted pseudoadiabatic lapse rate of 9.34°C km^{-1} generated by our model thus approaches the value for dry adiabatic ascent due to both the relatively small amount of latent heating possible at these cold temperatures and the consequences of cirrus cloud growth involving the freezing of haze particles below water saturation.

Concerning the factors that determine the concentrations of ice crystals nucleated within each generating pulse, the controlling mechanism is the balance between the rate of ice crystal production and the moisture release rate during the important initial part of the nucleation sequence. In other words, haze particle/ice crystal water vapor competition effects dominate the process. Therefore, updraft velocity exerts a strong influence on the concentrations of nucleated ice crystals (see Fig. 6) by modulating the impact of the initial vapor competition effects on nucleation as a function of the associated moisture release rate. The strong temperature dependence in the homogeneous freezing rate causes only a gradual increase in the ice crystal production rate with decreasing temperature (see Figs. 3 and 6) as a result of the tendency for solution droplet effects to normalize ice nucleation rates on the basis of an effective drop temperature. Finally, we note that although the total number of precipitated ice crystals varies with the amount of vertical wind shear (Fig. 5), this mainly reflects the relative frequency of generating pulses, and so is more dependent on the highly idealized framework of the one-dimensional model than the other parameters discussed above.

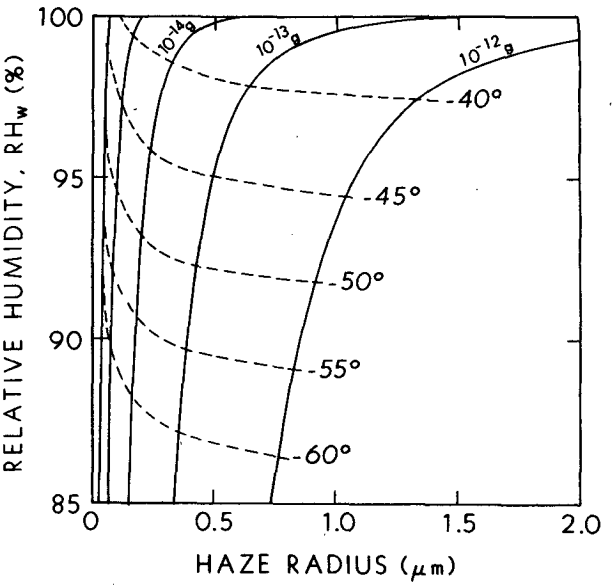

FIG. 11. The dependence on relative humidity of equilibrium haze particle sizes for the five ammonium sulfate CCN masses, shown as the solid lines. The intersections of the solid and dashed curves represent the maximum sizes of haze particles that would likely remain unfrozen, at least briefly, at the indicated temperatures.

5. Haze particle scattering and lidar applications

A primary motivation for these numerical experiments has been to test the hypothesis that the lidar linear depolarization ratio δ at the 0.694 μm ruby laser wavelength is sensitive to the presence of haze particles within cirrus. This has been suggested by lidar measurements of 0.2–0.3 δ values, which are uncharacteristically low for typical ice clouds but appropriate for mixed-phase cloud conditions, associated with cirrostratus cloud generating regions identified on the basis of Doppler radar, lidar backscattering, and aircraft data (Sassen et al. 1989). Moreover, arrays of relatively small cloud parcels displaying low δ values were associated with sheared precipitation trails, a characteristic that is obviously similar to the effects produced by the pulse-like generation of ice particles in our model predictions. Thus, it remains to be shown whether the scattering properties of growing haze particles capable of surviving, at least momentarily, before freezing homogeneously in an updraft are favorable for lidar detection. Another consideration is the amount of coexisting ice mass present, since the lidar depolarization technique senses a measure of cloud ice/water blance. It has already been shown, however, that relatively significant haze mass contents can exist only in regions devoid of ice particles and, as illustrated in Fig. 11, it is now possible to specify the maximum sizes of stable haze particles as a function of cloud temperature in order to calculate their backscattering properties.

Given in Fig. 11 is the dependence of ammonium sulfate equilibrium haze particle radii on relative humidity for the five CCN masses. (Note that the equilibrium haze sizes are based on a −40°C temperature, but little temperature dependence is present in this parameter over the range simulated.) The dashed lines present the maximum sizes of the particles before homogeneous freezing would likely occur at the indicated temperatures, according to Fig. 9. Figure 12 expresses these findings in terms of the ruby lidar backscattering gain G (equal to the single particle backscattering cross section divided by the particle area) for haze particles in the 0.1 to 1.5 μm radius range. These Mie scattering predictions, which have been smoothed to remove the resonance structure present in this region, are based on calculations at the four indicated refractive indices for pure water ($n = 4/3 - i0$) and at the increasingly higher indices corresponding to the approximate molalities at which the particles freeze at −40°, −50°, and −60°C. Clearly, droplet solution effects have the potential for significantly increasing the backscattering efficiency of particles in the important 0.5–1.0 μm range, which for pure water at the ruby laser wavelength represents a weakly scattering region in relation to the large-particle geometrical optics limit (arrows at $G \approx 1.3$).

Unfortunately, however, with our uncertain knowledge of CCN characteristics in the upper troposphere, it is difficult to speculate on the microphysical properties corresponding to a threshold of cloud haze/ice balance favorable for lidar detection. Nonetheless, it is relatively simple to demonstrate that significant decreases in depolarization can be attributed to haze particles in a diffuse ice cloud. For example, we can treat

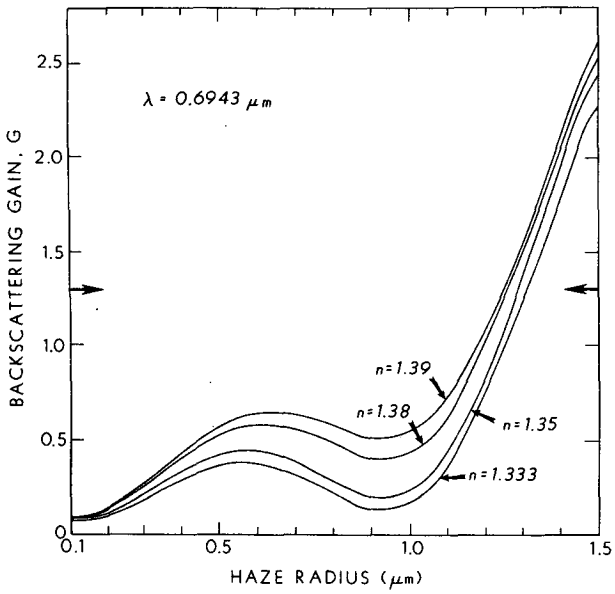

FIG. 12. Comparison of smoothed backscattering gains from Mie scattering theory at the ruby laser wavelength λ for pure water, and haze particles with the increasing refractive indices caused by increases in the molality of the ammonium sulfate solution. Arrows at $G = 1.3$ show the geometric optics limit for large particles.

the case where the $\delta = 0.4$ value for a pure ice cloud is reduced to $\delta = 0.25$ from haze particle scattering (see Sassen and Dodd 1988). Using the appropriate backscattering gains from Fig. 12 for haze radii of 1.0, 0.5, and 0.25 μm, the 0.25 δ value can be achieved for haze particle concentrations of approximately 0.1, 0.3, or 4.0 cm^{-3} at these sizes, respectively, in the presence of 100 μm long column crystals at a concentration of 0.1 l^{-1}. It does not seem unreasonable to assume that such conditions could be briefly encountered in cirrus generating regions.

6. Conclusions

The microphysical and laser scattering properties of cirrus cloud generating regions have been studied using a mixed-phase hydrometeor growth model that incorporates a highly idealized precipitation mechanism dependent on vertical wind shear. The range of temperatures considered is −35° to −60°C, the regime in which the homogeneous drop freezing mode likely dominates ice crystal nucleation. The main findings from these simulations can be summarized as follows:

1) Ice crystal production in a uniform updraft is accomplished in a pulse-like fashion from the homogeneous freezing of haze particles, whose equilibrium sizes fluctuate in response to the water vapor competition effects produced by the ice crystals nucleated. Ice crystal concentrations increase with increasing vertical velocity due to the lessening impact of haze/ice particle vapor competition effects (at the start of the nucleation sequence) during more rapid adiabatic expansion.

2) Ice crystal nucleation in the generating pulse occurs under prescribed environmental conditions for a given CCN population, where the required relative humidity with respect to water gradually decreases with decreasing temperature. Water saturation is not required for ice nucleation at temperatures $\leqslant -35°C$, and thus this temperature marks a discontinuity in the conditions required for cloud formation in the troposphere. In effect, the likelihood of cirrus cloud formation increases with decreasing temperature, insofar as reduced humidities are required.

3) As a corollary of (2), with decreasing temperature precipitation production becomes increasingly smaller than that possible from a pseudoadiabatic process involving nucleation at water saturation. For example, accumulated ice mass content differences are ~15% as a temperature of −60°C is approached.

4) The higher refractive indices associated with solution droplets enhance the likelihood of haze particle detection by lidar probing. Decreases in the linear depolarization ratio for visible-wavelength lidars within cirrus should be noticeable in the type of ice generating regions simulated here. Ammonium sulfate CCN masses of $\geqslant 10^{-14}$ to 10^{-13} g favor lidar detection.

Of course, our simplistic treatment of a uniform updraft in a uniformly sheared environment forces the simulation of a regular sequence of ice generating pulses, which would not likely be maintained in atmospheric cirrus clouds for prolonged periods of time. Obviously, the effects of variable or sporadic updrafts, and variable background ice crystal concentrations, would not generate such tidy results. Nonetheless, the basic findings summarized above would still generally be applicable. As can be seen by the equations inserted in Fig. 1, the model framework accommodates a certain amount of scaling between the model input parameters of vertical wind shear, and updraft velocity and radius, such that the basic model findings may reflect a wider range of conditions in cirrus than have been simulated here. (For example, a tenfold increase in vertical velocity is compensated for by a reduction in the impulse radius of from 500 to 50 m to yield the same critical fall distance z_c.) Furthermore, despite the fact that errors may exist in the droplet freezing rate employed here, the basic nucleation behavior of haze particles within cirrus would not be altered.

These basic cloud microphysical findings regarding cirrus ice particle generation are in broad agreement with the model results obtained by Heymsfield (1973, 1975) for cirrus uncinus, despite differences in the treatment of the homogeneous freezing of ammonium sulfate haze particles. Although clearly a model with a two-dimensional framework would provide a more suitable foundation for studying many aspects of cirrus cloud formation, one-dimensional modeling studies

can be applied to comprehending specific cloud properties. A chief goal has been to develop a parametric treatment of new ice particle generation, on the basis of detailed microphysical simulations, for incorporation in improved cirrus cloud growth models. For example, recent large-scale cirrus numerical studies (Starr and Cox 1985; Starr 1987) have involved the application of a time-dependent, two-dimensional Eulerian model, with generalized cloud microphysical parameterizations drawn from experimental findings. Designed to investigate the basic role of various physical processes in the growth and maintenance of cirrus, the model employed a grid resolution of 100 m and a time step of 30 s. In computing the ice-versus-vapor phase changes, the ice mass content was linked to the maintenance of relative humidity with respect to ice (RH_i) of 105%; ice growth occurred both with regard to the introduction of new particles and the growth of existing particles. To initiate ice particle formation in regions devoid of ice particles, a RH_i of 120% was required.

In contrast, the findings shown in Fig. 9 can be used to provide a relatively simple parametric treatment of ice particle nucleation that reflects the action of realistic microphysical processes. For this purpose, we introduce the relation

$$RH_w = (5.36 \times 10^{-3})T(K) - 0.276,$$

to describe the temperature dependency of relative humidity required for the introduction of new ice crystals for temperatures $\leqslant -35°C$. In effect, cirrus cloud processes follow an adjusted pseudoadiabat, although for temperatures $\geqslant -35°C$, the $\sim 100\%$ relative humidity barrier is appropriate. This equation is derived from a linear fit to the solid circles from Fig. 9, and was used earlier to compute the solid accumulated precipitation mass curve in Fig. 10. The choice of this relation represents our appraisal of the threshold conditions for ice nucleation in cirrus, and although dependent on CCN mass and updraft velocity, the shifts in the curves induced by these factors are relatively minor over the range of conditions simulated. It should also be pointed out that significant improvements in the model time step, and in computation time, can be realized by assuming that the haze particles always maintain their equilibrium sizes (solely a function of RH_w for a given CCN mass, to a good approximation), and by binning ice crystal sizes, without impacting significantly on the model predictions.

In conclusion, it would appear that the influence of haze particles on cirrus clouds is significant enough to warrant basic airborne and laboratory research efforts directed toward increasing our understanding of the nature and microphysical effects of CCN in the upper troposphere. In addition to the effects described here on ice particle nucleation and lidar depolarization, the presence of a relatively significant equilibrium haze component (in comparison to the rather low ice mass contents typically measured in "cold" cirrus) may represent a radiatively important constituent, both with regard to shortwave cloud optical thickness, and to the possible increased absorption of solar radiation, a characteristic common among hazes.

Acknowledgments. This research was supported by Grant ATM-85 13975 from the National Science Foundation. The authors would like to thank D. O'C. Starr and N. Fukuta for helpful discussions.

REFERENCES

Davis, C. I., 1974: The ice-nucleating characteristics of various AgI aerosols. Ph.D. dissertation, University of Wyoming, 267 pp.

Hall, W. D., and H. R. Pruppacher, 1976: The survival of ice particles falling from cirrus clouds in subsaturated air. *J. Atmos. Sci.*, **33**, 1995–2006.

Heymsfield, A. J., 1973: The cirrus uncinus generating cell and the evolution of cirriform clouds. Ph.D. dissertation, University of Chicago, 269 pp.

——, 1975: Cirrus uncinus generating cells and the evolution of cirriform clouds. Part II: The structure and circulations of the cirrus uncinus generating head. *J. Atmos. Sci.*, **32**, 809–819.

——, 1977: Precipitation development in stratiform ice clouds: A microphysical and dynamical study. *J. Atmos. Sci.*, **34**, 367–381.

Platt, C. M. R., and A. C. Dilley, 1981: Remote sounding of high clouds. Part IV: Observed temperature variations in cirrus optical properties. *J. Atmos. Sci.*, **38**, 1069–1082.

Sassen, K., and G. C. Dodd, 1988: Homogeneous nucleation rate for highly supercooled cirrus cloud droplets. *J. Atmos. Sci.*, **45**, 1357–1369.

——, D. O'C. Starr and T. Uttal, 1989: Mesoscale and microscale structure of cirrus clouds: Three case studies. *J. Atmos. Sci.*, **46**, 371–396.

Starr, D. O'C., 1987: Effects of radiative processes in thin cirrus. *J. Geophys. Res.*, **92**, 3973–3978.

——, and S. K. Cox, 1985: Cirrus clouds. Part II: Numerical experiments on the formation and maintenance of cirrus. *J. Atmos. Sci.*, **42**, 2682–2694.